nature communications

Article

https://doi.org/10.1038/s41467-026-72822-w

# A squirrel-inspired drone with enhanced stability, agility and maneuverability via whole-body morphing

Received: 16 April 2025

Accepted: 20 April 2026

Published online: 13 May 2026

Check for updates

Liming Zheng (郑黎明)[1], Alexander van Zuijlen[2] & Salua Hamaza[1]

Gliding mammals, such as flying squirrels, exhibit remarkable flight abilities by dynamically controlling their wing membranes (patagia), using their limbs and tail to manoeuvre between trees. They achieve agile and manoeuvrable gliding by adjusting their body and wing shape to control trajectory and stability. While research on bio-inspired drones primarily focuses on avian flight, the aerodynamic implications of whole-body morphing paired with soft membrane deformations in mammalian gliders remain unexplored. To address this, we developed the SquirrelDrone, a bioinspired drone capable of continuously modulating its shape via limb and tail actuation, coupled with passive deformations of its skin-like membrane. This design enables the investigation of how coordinated limb motion and membrane morphing affect aerodynamic forces during flying. Wind-tunnel and flight experiments show that gliding-mammal-inspired morphing significantly improves drone stability, agility, and manoeuvrability, providing a bioinspired framework for understanding how whole-body morphing contributes to flight control in future morphing aircraft.

Unlike birds, which morph their wings using feathers[1,2] and generate lift through flapping[3], gliding mammals possess a distinct ability to morph their soft-membrane body to maneuver smoothly while gliding through complex forest environments. These mammals form a diverse group capable of effortlessly navigating from tree to tree[4] by launching from the upper branches or trunk, and extending their specially adapted gliding membranes, known as patagia, which stretch from their forelimbs to their hindlimbs along the sides of their body. This adaptation allows them to glide silently through the night air over considerable distances, and some species can cover more than 100 meters in a single glide[4]. During these manoeuvrers, they can twist and turn to avoid obstacles and make precise landings on target trees[5].

The secret behind the remarkable morphability of gliding mammals lies in their elastic patagium, or gliding membrane[5]. Biologically, there are four types of patagia: the *plagiopatagium, propatagium, uropatagium*, and *digipatagium* (see Fig. 1c). The *plagiopatagium*, or flank membrane (Fig. 1c.A), is the primary gliding membrane found in all gliding mammals. It extends between the forelimbs and the hindlimbs and is under precise muscular control. The *propatagium* (Fig. 1c.B), or neck membrane, attaches on each side of the neck and along the anterior edge of the forelimbs. This patagium is most developed in colugos and is little developed, or absent, in other gliding mammals. The *uropatagium* (Fig. 1c.C), or tail membrane, stretches between the posterior surface of the hind legs and the tail, and is found only in larger gliding mammals weighing over approximately 1 kg[5], see Fig. 1e green part. Lastly, the *digipatagia* (Fig. 1c.D), exclusive to colugos, consist of membranes spanning the spaces between each of the five digits on both the front and hind feet, see Fig. 1e yellow part.

Biological organisms demonstrate remarkable capabilities in agile flight. Both birds and gliding mammals can safely navigate through cluttered environments thanks to their exceptional agility and maneuverability. In aerospace engineering, agility[1,6] is typically defined as

[1]BioMorphic Intelligence Lab, Department of Control & Operations, Faculty of Aerospace Engineering, TU Delft, Delft, The Netherlands. [2]Aerodynamics, Department of Flow Physics and Technology, Faculty of Aerospace Engineering, TU Delft, Delft, The Netherlands. e-mail: L.Zheng-1@tudelft.nl; S.Hamaza@tudelft.nl

https://doi.org/10.1038/s41467-026-72822-w

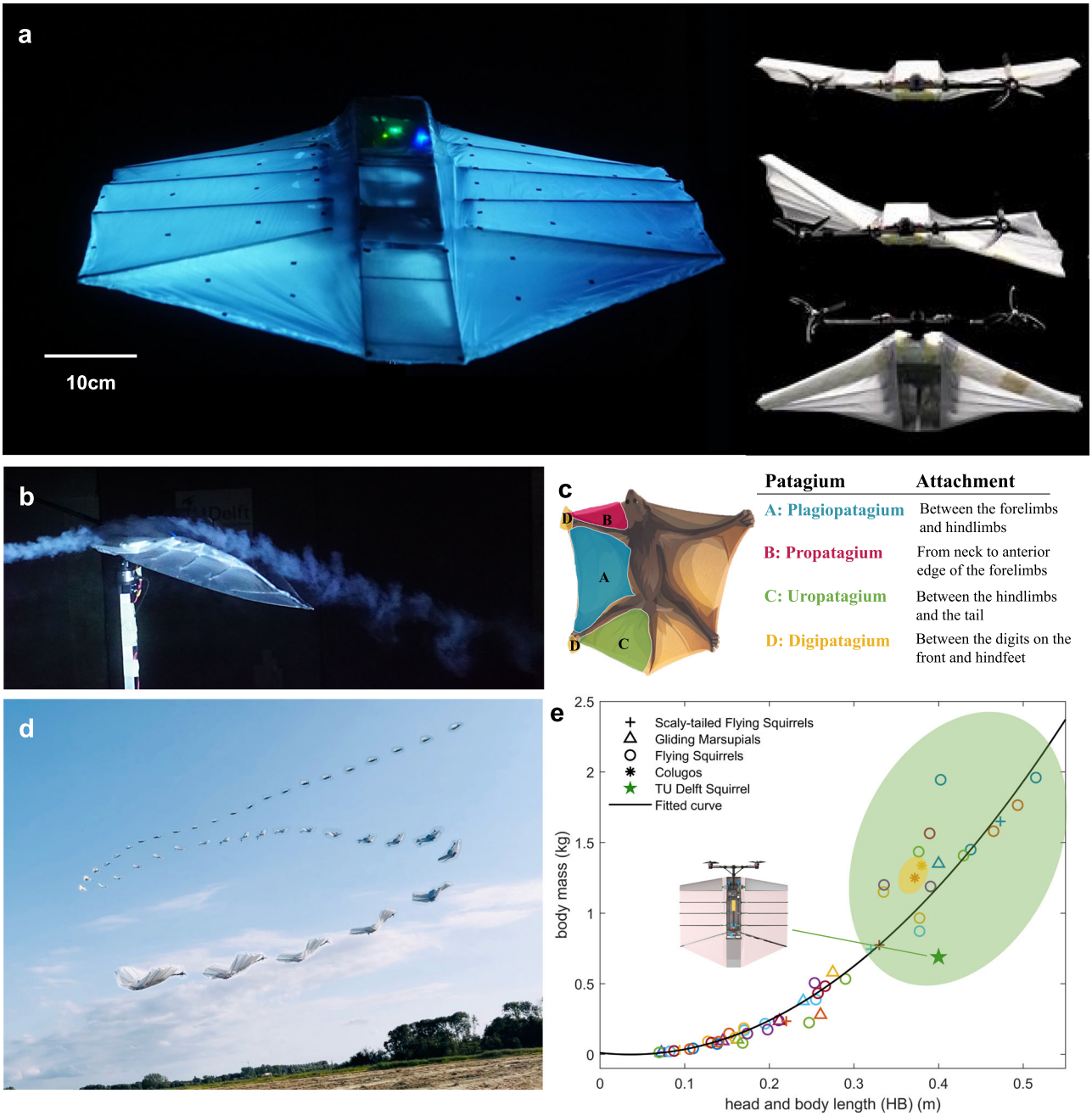


**Fig. 1 | Gliding mammals and SquirrelDrone. a** The SquirrelDrone with whole-body morphing configurations (see Supplementary Movie 6). **b** The SquirrelDrone during wind tunnel testing. **c** The distribution and naming of the patagium in gliding mammals. **d** Agile trajectories conducted on SquirrelDrone in outdoor tests (see Supplementary Movie 1). **e** Relationship between the head and body length (HB, from the tip of the snout to the cloaca along the ventral surface) and weight among 53 species of gliding mammals[5]; the black solid line represents the fitted curve. The green star denotes the design of the SquirrelDrone. The green area indicates species with a *uropatagium*, and the yellow area denotes species with a *digipatagium*. Source data are provided as a Source data file.

the ability to change orientation rapidly, often enhanced by large aerodynamic control surfaces capable of generating strong moments. For biological flyers, high agility allows rapid attitude adjustments to avoid imminent collisions. Maneuverability[1,7], in contrast, refers to the ability to change velocity, or more specifically, to alter the flight trajectory. It depends on the range and magnitude of available aerodynamic and propulsive forces, where greater lift and drag authority enable sharper acceleration or deceleration.

In conventional fixed-wing aircraft, both agility and maneuverability are constrained by fixed aerodynamic configurations and remain essentially constant once the aircraft is designed. Consequently, their dynamic response and control authority can be modified only with marginal changes in flight. In contrast, biological flyers can continuously and drastically reshape their body and wings to actively regulate these properties in response to environmental demands. This inherent flexibility enables transitions between stable and agile flight states, providing an adaptive balance between stability, agility, and maneuverability. For small aerial vehicles, achieving high aerodynamic performance, stability, maneuverability, and agility simultaneously within limited size and weight constraints remains a central design challenge.

To overcome these limitations, engineers have increasingly drawn inspiration from nature, developing a broad range of morphing-wing drones that mimic biological flyers. By adjusting parameters such as

https://doi.org/10.1038/s41467-026-72822-w

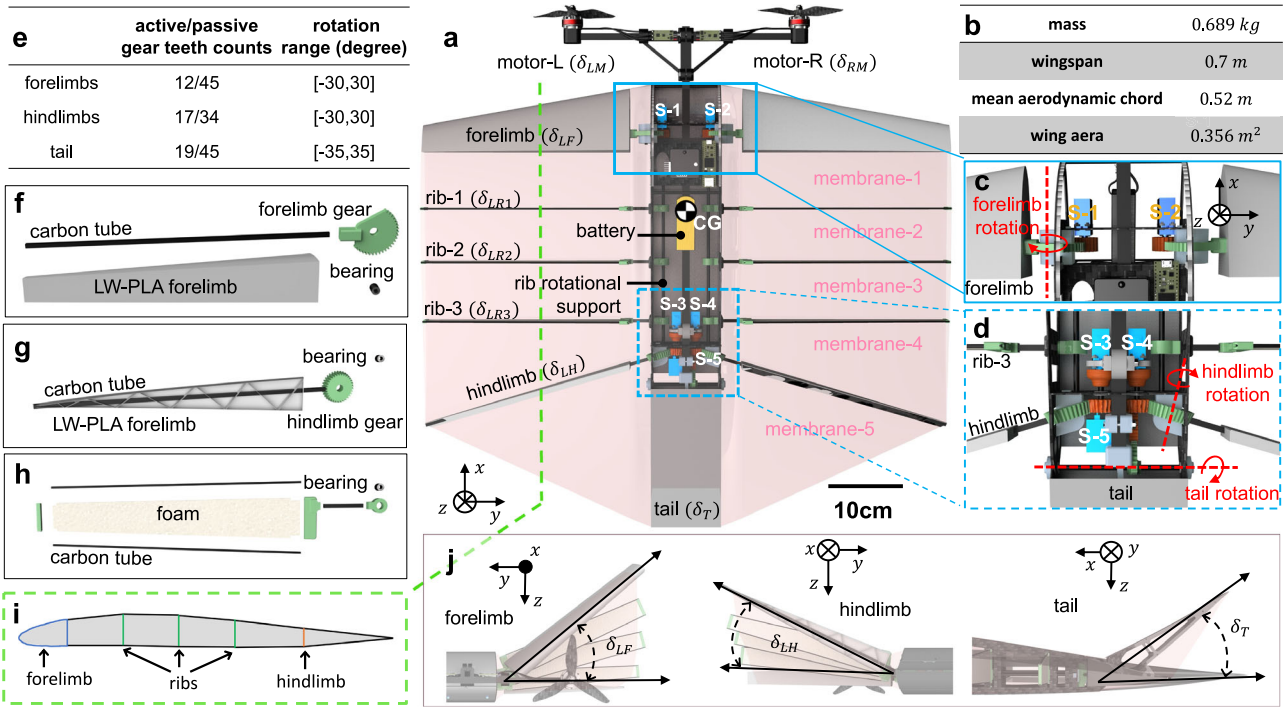


**Fig. 2 | Morphing wing drone architecture. a** Top view of the SquirrelDrone, showing the layout of the forelimb, ribs, hindlimb, tail, body, propulsion system, transmission mechanisms, membrane segmentation, and definitions of rotation angles for each component. **b** Parameters of SquirrelDrone. **c** Details of the forelimbs gear-driven mechanism. **d** Details of the gear-driven mechanisms for the hindlimbs and tail. **e** Gear teeth counts and rotation ranges of the forelimbs, hindlimbs, and tail. **f**–**h** Structural components of the forelimbs, hindlimbs, and ribs. **i** Wing cross-section at 200 mm from the symmetry plane. The baseline NACA M5 airfoil is shown in gray, the forelimb in blue, ribs in green, and the hindlimb in orange. **j** Definition of positive angle deflections for the forelimbs, hindlimbs, and tail.

wing sweep, span, chord, out-of-plane twist, dihedral angle, and airfoil camber or thickness, researchers have created aerial platforms that can actively modify their aerodynamic characteristics in flight[8,9]. For example, bird-inspired drones such as PigeonBot[2,10] and LisHawk[1,11] achieve continuous shape and surface-area changes by reconfiguring feather overlays, thereby improving control authority and expanding their flight envelope. By dynamically adjusting the effective areas of wings and tails, these drones can tune the distance between the center of gravity and the aerodynamic center to regulate longitudinal stability. Furthermore, twisting tails have been shown to enhance lateral stability and suppress Dutch roll[10,11], while also improving yaw control authority. Introducing wing twist further enables smooth aerodynamic transitions without relying on discrete control surfaces, improving flight performance by modulating the effective angle of attack to control body orientation[12–14]. In addition, bat-inspired platforms such as BatBot[15] utilize compliant membrane wings that passively adapt to airflow, reproducing key aerodynamic features of bats and enhancing lift generation during low-speed gliding.

In this work, we present a soft membrane-based shape-morphing drone—SquirrelDrone—inspired by the flight mechanics of gliding mammals (see Supplementary Movies 5 and 8). Retaining the essential *plagiopatagium*, *propatagium*, and *uropatagium* (Fig. 1), this system employs actively controlled fore- and hindlimbs and a tail, along with passively controlled ribs to achieve whole-body morphing. We show that the drone adapts its wing camber in response to differential pressure across its soft surfaces, which improves lift performance and longitudinal stability. Furthermore, through the coordinated movement of the forelimbs and hindlimbs, the system actively modulates wing camber and angle of attack, enhances lateral stability, and delays stall. By embodying the anatomical intelligence of gliding mammals, we demonstrate that whole-body morphing significantly enhances maneuverability and agility, enabling dynamic and precise flight in complex environments.

## Results

### The robotic gliding mammal

The *plagiopatagium*, *propatagium*, and *uropatagium* are the most important components that form the gliding surface. All gliding mammals possess a *plagiopatagium*, which constitutes the main portion of the wing area[5]. According to the lift equation (see Eq. (2))[16], larger wing areas allow for greater payload capacity for aircraft in level flight. The aspect ratio of gliding mammals is between 1.0 and 2.2[17]. By analysing the head and body length (HB, measured from the tip of the snout to the cloaca along the ventral surface) and body mass of 53 species of gliding mammals[5], we demonstrate the quadratic relationship between HB and body mass, as depicted by the black solid line in Fig. 1e, with the Eq. (1). The *propatagium* increases the wing's sweep angle, which can reduce the risk of wingtip stall and improve the aircraft's lateral stability[18]. *Uropatagium* appears in large gliding mammals (see Fig. 1e green part), where the tail is round and fluffy rather than flat, to increase the pitch extension. Colugos instead incorporate the tail within the membrane, further increasing the wing area. Inspired by those, we designed the SquirrelDrone as a tailless flying wing with morphing limbs and tail incorporated in the soft patagia-like membrane (see "Biomimetic scaling of aerodynamic parameters" in Methods and Parameters in Fig. 2b).

The patagia consist of the skin with two layers bound tightly together by connective tissue, with muscles and nerves in between[19], forming a thin airfoil that can be easily retracted when not gliding. To improve aerodynamic performance, we add three ribs between the two layers of the SquirrelDrone's wing membrane (0.01 mm) to create a thicker airfoil (see Fig. 2h, i). Compared to a thin airfoil, a thicker airfoil has a larger leading-edge radius, reducing flow separation and delaying stall[20]. This design also provides space for electronic components and improves structural reliability.

Gliding mammals initiate flight by leaping from the tops of the trees to gain velocity and acceleration, then extend their forelimbs

https://doi.org/10.1038/s41467-026-72822-w

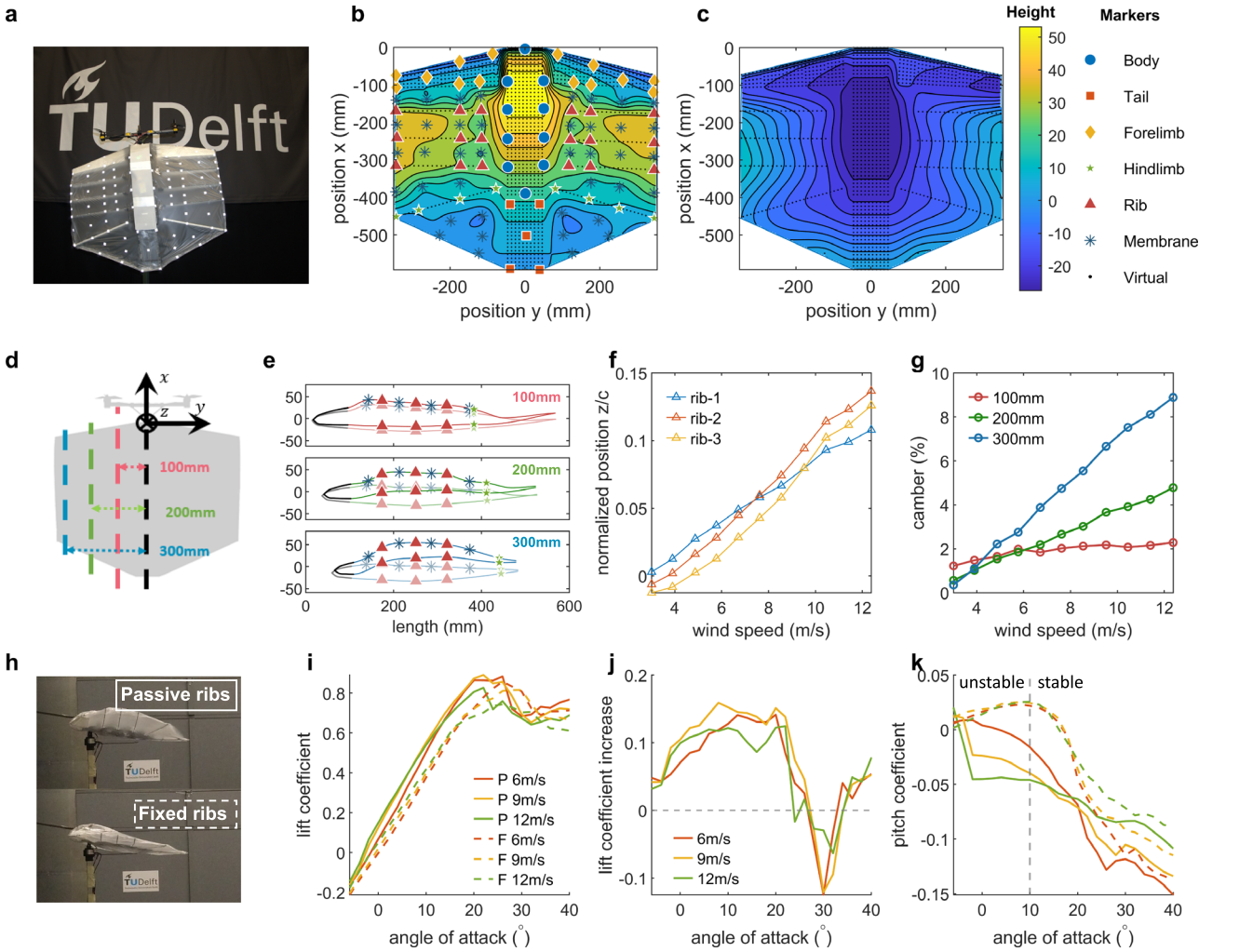


**Fig. 3 | Passive membrane morphing increases lift performance and pitch stability. a** An array of reflective markers used on the upper wing surface area to capture the high morphability of SquirrelDrone. **b** Upper surface of the morphing body at 9 m/s and 10° angle of attack, showing both real and virtual markers (black dots) generated from CAD models. **c** Lower surface illustrating virtual markers derived from the upper surface markers. **d** Airfoil sections at 100 mm, 200 mm, and 300 mm from the symmetry plane, color-coded in red, green, and blue, respectively. **e** Comparative airfoil profiles at 0 m/s and 9 m/s, depicted in light and dark shades, highlighting the positions of limb and rib markers. **f** Normalized vertical elevation $z/c_{300}$ of the ribs at $y = 300$ mm under different wind speeds, where $c_{300}$ is the local chord length at $y = 300$ mm. **g** Camber variations at the three specified sections under different wind speeds. **h** Two configurations: fixed ribs versus passively morphing ribs. **i** Comparison of lift between F (fixed ribs) and P (passive ribs) across different angles of attack and wind speeds. **j** Increase in lift coefficient of passive ribs compared to fixed ribs. **k** Comparison of pitch moment coefficients; the fixed-rib configuration exhibits longitudinal static instability at angles of attack below 10°. Source data are provided as a Source data file.

forward and hindlimbs backward to fully deploy the patagia[21]. Their limbs can rotate in multiple directions, with vertical rotation playing a key role in modulating wing shape and flight attitude[22,23]. Inspired by this mechanism, the SquirrelDrone implements a simplified morphing system that allows vertical rotation only, enabling active modulation of wing camber, twist, and dihedral. To reduce mechanical complexity while preserving a large effective wing area, the forelimbs, hindlimbs, and tail are actuated by five servos (S-1 to S-5; Fig. 2a), with rotation angles constrained between −30° and 30° for the limbs, and −35° to 35° for the tail (Fig. 2e, j).

Unlike gliding mammals that rely on passive descent, the SquirrelDrone performs fully powered flight using two front-mounted propellers to gain altitude and sustain accelerated flight. These motors provide continuous thrust and enable controlled maneuvers under varying aerodynamic loads. Limb and tail rotations deform the compliant membrane-based wings in real time (Fig. 2j), allowing the vehicle to dynamically adapt its morphology in powered flight.

The soft membrane enables morphing to different shapes through the actuation of these five components. To maintain the aerodynamic shape and structural integrity of the membrane during morphing, three ribs stretch between the forelimb and hindlimb (three per wing). The wing cross-section is based on a NACA M5 airfoil with an S-shaped profile (Fig. 2i). At 200 mm from the symmetry plane (green dashed line in Fig. 2a), the section illustrates the baseline NACA M5 profile in gray, the forelimb leading edge in blue, rib positions in green, the hindlimb in orange, and the soft membrane in black. The forelimbs and hindlimbs are actively rotated vertically by the servos, while the ribs move passively with the membrane. The final shape results from the combined influence of limb and tail angles and aerodynamic loading, forming the SquirrelDrone's morphing strategy.

## Passive deformation of the skin-like membrane enhances lift and pitch stability

To assess the important contribution of passive body morphing provided by the skin-like soft membrane, we conducted experiments in a

wind tunnel (see 'Membrane-based deformation tracking' in Methods). We placed a total of 95 reflective markers on the upper surface of the wings (see Fig. 3a), and the known location of the rigid limbs forming the skeleton of the Squirrel, we generated an additional 2560 virtual markers to reconstruct both the upper (see Fig. 3b) and lower (see Fig. 3c) surfaces of the soft membrane wing. To quantify the deformation induced by the passive ribs, we defined the normalized rib displacement as the upward shift $z$ of the rib position relative to the baseline NACA M5 airfoil at construction, normalized by the local chord length $c_{300}$. At rest, the ribs sag downward under gravity. As wind speed increases, however, the low-pressure region forms on the upper surface, pulling the ribs upward (see details in Supplementary Fig. 1). At a wind speed of 12 m/s, the ribs elevated by approximately 10% to 13% of the chord (Fig. 3f). This upward displacement results in an increase in airfoil camber (see "Camber and chord measurement" in Methods). Because ribs located further from the wing root are also further from the rotation axis, they exhibit larger upward displacements, leading to more pronounced camber variation (Fig. 3e, g). Notably, the camber increases more significantly towards the wingtips, with increments of about 1.1%, 4.8%, and 8.9% at 100 mm, 200 mm, and 300 mm from the root, respectively.

To evaluate the aerodynamic benefits of passive rib deformation, we conducted wind tunnel experiments with ribs in two configurations: passive and fixed (Fig. 3h). In the passive configuration, the ribs were free to rotate under aerodynamic loading, thereby altering the local chord-wise camber. In the fixed configuration, the relative position of the ribs was constrained, keeping them in their initial orientation. Both configurations were tested at wind speeds of 6, 9, and 12 m/s across a range of angles of attack from −6° to 40°, with measurements of lift (Fig. 3i) and pitch coefficient (Fig. 3k). The results show that the passive rib configuration consistently produced higher lift, particularly at angles of attack below 24° (Fig. 3i, j). In this regime, the lift coefficient increased by more than 0.1 compared to the fixed-rib case. This enhancement can be attributed to the increased camber induced by the upward deflection of the passive ribs, which strengthens the circulation around the airfoil and increases the pressure difference between the upper and lower surfaces, thereby generating greater lift. At angles above 24°, flow separation on the upper surface caused oscillations of the passive ribs, resulting in a marked reduction of lift below that of the fixed-rib configuration. Once the flow stabilized, however, the passive configuration again recovered to higher lift levels after 35°.

Additionally, the fixed-rib configuration—similar to a conventional fixed wing—exhibited longitudinal static instability at angles of attack below 10° (center of gravity located at 31% of the mean aerodynamic chord). It only attained longitudinal static stability (see "Longitudinal stability" in Methods) once the angle of attack exceeded 10°. In contrast, the passive configuration maintained longitudinal static stability across the entire tested range. The camber increase induced by the passive ribs not only improved lift performance but also generated additional nose-down pitching moments, thereby enhancing longitudinal stability at low angles of attack. The transition point observed at negative angles of attack (Fig. 3k, solid lines) corresponds to the shift from negative to positive camber, which produces a sudden increase in nose-down pitching moment (see Supplementary Fig. 1 and Supplementary Movie 2 for details). This demonstrates that the soft passive rib design of the SquirrelDrone simultaneously enhances lift and substantially improves longitudinal stability.

## Active whole-body morphing enhances lateral directional stability

Flying squirrels actively control the angles of their forelimbs, hindlimbs, and tail to reshape their soft-membrane body, thereby modulating aerodynamic forces and moments. In aerospace terminology, the forelimbs correspond to the leading edge (LE) and the hindlimbs to the trailing edge (TE). In conventional aircraft, the wing spar serves as the primary load-bearing structure and is typically fixed relative to the fuselage. By rotating the LE or TE about the spar, the wing twist can be adjusted, which in turn modifies the aerodynamic forces and moments[12,24–26]. Compared with conventional control surfaces, this distributed twisting mechanism produces continuous lift variations along the entire span without introducing abrupt surface discontinuities, thereby improving both control effectiveness and aerodynamic efficiency.

The SquirrelDrone adopts a similar strategy. By combining three actuation modes, the wing can generate pronounced twist: Mixer-1—forelimb actuation only (Fig. 4a, blue line), Mixer-2—hindlimb actuation only (Fig. 4b, red line), and Mixer-3—opposite-direction actuation of forelimbs and hindlimbs (Fig. 4c, yellow line). Using motion capture in the wind tunnel, we recorded the resulting wing deformations. The results show that all three twisting modes yield the highest airfoil camber near $\delta_{\mathrm{mix},n} = 0°$ (Fig. 4e). Forelimb and hindlimb actuation produced similar effects on the effective local airfoil angle (Fig. 4f, blue and red lines), whereas differential actuation of the two resulted in a substantially larger change (Fig. 4f, yellow line). In terms of aerodynamic performance, hindlimb actuation generated greater variations in both lift and drag compared with forelimb actuation, while differential actuation produced the largest changes among all modes (Figure 4g and h). This stronger aerodynamic response from the hindlimbs arises because they act further downstream along the chord, where a given angular deflection produces a larger geometric deformation of the trailing edge and greater modification of the local camber. In addition, the hindlimbs influence a region of the flow where separation and pressure recovery are more sensitive, leading to a stronger modulation of both lift and drag forces.

In aerospace engineering, the dihedral angle of a wing is commonly used to regulate lateral stability and maneuverability. Aircraft with a positive dihedral generate a restoring rolling moment in sideslip, thereby contributing to lateral static stability. This mechanism is an important feature in modern aircraft design for enhancing lateral stability. However, an excessively large dihedral can reduce maneuverability. Conventional fixed wings have a constant dihedral angle, and thus cannot balance lateral stability and controllability in real time. The SquirrelDrone, by contrast, can achieve variable dihedral—or even anhedral—through synchronous rotation of the forelimbs and hindlimbs by equal angles (see Fig. 4d, green line). Wind tunnel observations revealed that increasing dihedral reduces chordwise airfoil camber. This occurs because the upper and lower membranes are attached to the dorsal and ventral sides of the fuselage, respectively: in the anhedral state, the lower membrane relaxes while the upper membrane is tensioned, pulling the ribs upward and thereby increasing camber. In the dihedral state, the ribs are subjected not only to upward aerodynamic loading but also to a downward force from the tensioned lower membrane, resulting in reduced camber. During dihedral morphing, the effective local airfoil angle (Fig. 4f green line) remains nearly constant because the fore- and hindlimbs rotate by the same angle. Consequently, the aerodynamic effects are dominated by camber variation, with both lift and drag coefficients decreasing progressively as the dihedral angle increases.

Variations in wing twist and dihedral influence both lateral and directional stability. To evaluate lateral stability, we used the roll stability derivative $C_{l\beta}$ (see "Lateral and directional stability" in Methods), defined as the slope of the rolling moment coefficient $C_l$ with respect to the sideslip angle $\beta$. A more negative $C_{l\beta}$ indicates greater lateral stability. Directional stability was assessed using the weathercock stability derivative $C_{n\beta}$ (see "Lateral and directional stability" in Methods), the slope of the yawing moment coefficient $C_n$ with respect to $\beta$; values below zero correspond to static directional stability. Wind tunnel balance measurements were conducted at fixed angles of attack over a range of sideslip angles ($\beta$), from which $C_{l\beta}$ and $C_{n\beta}$ were

https://doi.org/10.1038/s41467-026-72822-w

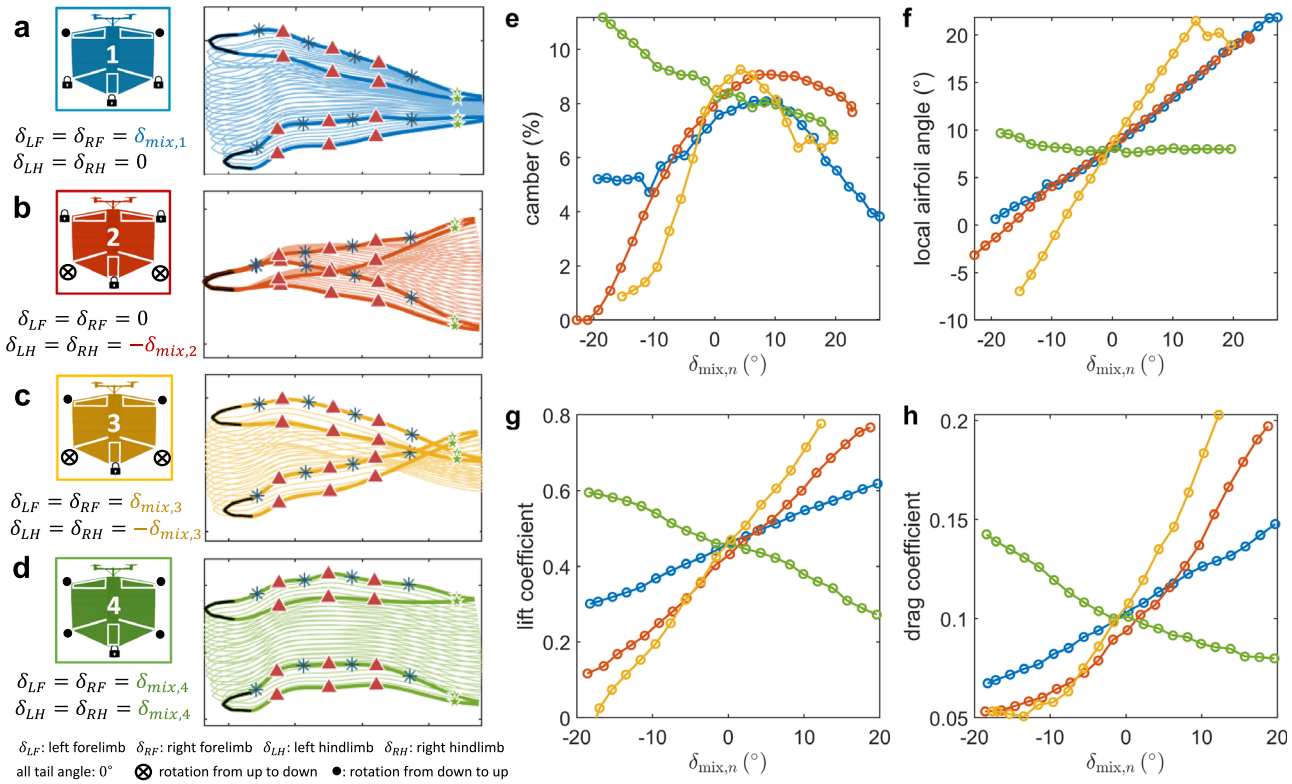


**Fig. 4 | Active whole-body morphing through multi-limb actuation. a** Mixer-1 strategy: forelimbs only. All actuators rotate upward in the positive direction, including $\delta_{LF}$, $\delta_{RF}$, $\delta_{LH}$, and $\delta_{RH}$. The right panel illustrates the airfoil deformation at the 300 mm spanwise location as $\delta_{\mathrm{mix},n}$ varies from −20° to 20°. The initial and final profiles are highlighted, with ribs, membrane, forelimbs, and hindlimbs annotated (symbols consistent with Fig. 3b, c). **b** Mixer-2 strategy: hindlimbs only. **c** Mixer-3 strategy: forelimbs and hindlimbs rotate in opposite directions. **d** Mixer-4 strategy: forelimbs and hindlimbs rotate in the same direction. **e**–**h** Corresponding variations in camber, local airfoil angle, lift coefficient, and drag coefficient. Source data are provided as a Source data file.

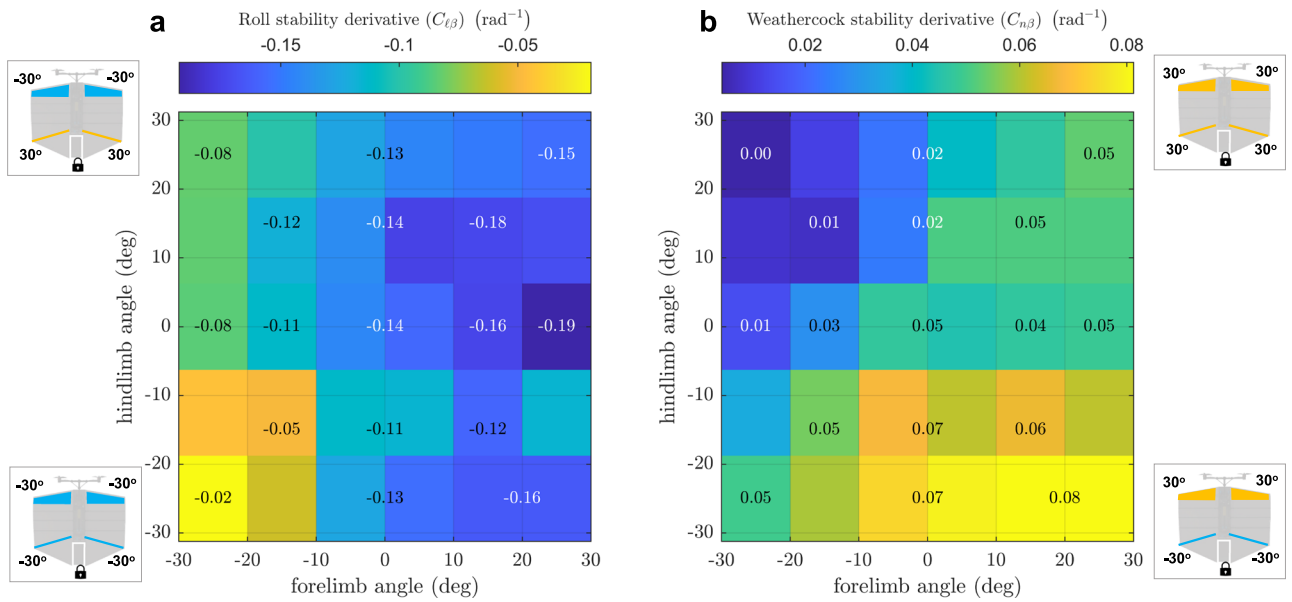


**Fig. 5 | Active whole-body morphing enhances lateral stability. a** Roll stability derivative ($C_{l\beta}$) at an angle of attack of 10° for symmetric morphing of the forelimbs and hindlimbs. **b** Weathercock stability derivative ($C_{n\beta}$) at an angle of attack of 10° for symmetric morphing of the forelimbs and hindlimbs. Source data are provided as a Source data file.

extracted at $\beta$ = 0°. Multiple combinations of forelimb and hindlimb configurations were tested, and the results are shown in Fig. 5. Actuating the forelimbs alone produced larger improvements in roll stability than actuating the hindlimbs alone. Overall, both increased dihedral ($C_{l\beta}$ decreasing from −0.02 to a minimum of −0.18) and increased twist ($C_{l\beta}$ decreasing from −0.08 to a minimum of −0.16) enhanced lateral stability (Fig. 5a).

The SquirrelDrone, however, exhibited directional instability across all tested configurations, which motivated the inclusion of two front-mounted propellers in the design (Fig. 2a). By adjusting the

https://doi.org/10.1038/s41467-026-72822-w

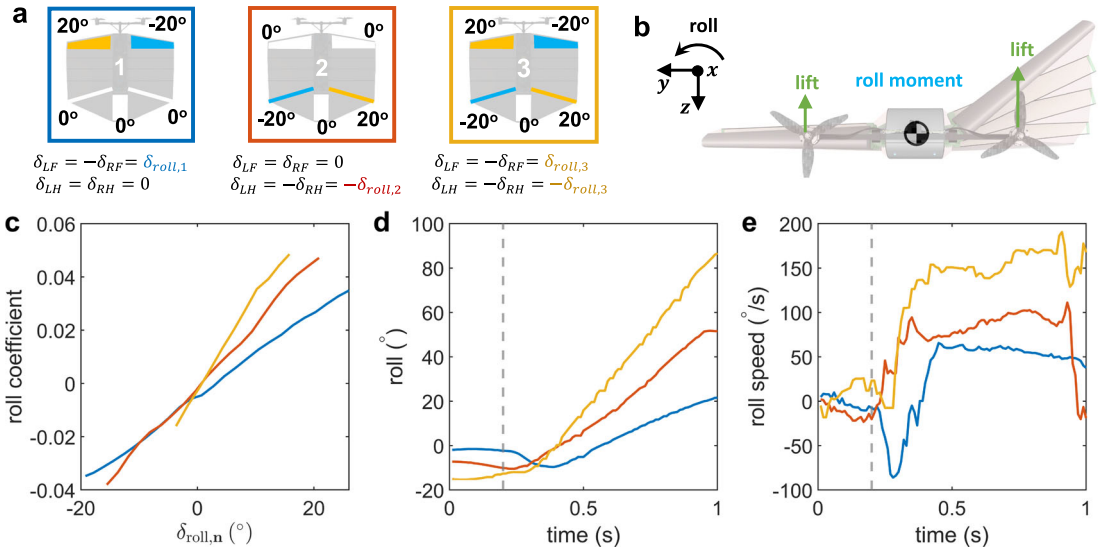


**Fig. 6 | High morphability enhances roll agility. a** Open-loop dynamics were tested in the wind tunnel at 9 m/s under asymmetric wing morphing (see "Open-loop dynamic flight test in wind tunnel" in Methods). Three experimental configurations were applied: forelimb actuation only (blue), with hindlimbs and tail fixed at 0° (left forelimb +20°, right forelimb −20°); hindlimb actuation only (red), with forelimbs and tail fixed at 0° (left hindlimb −20°, right hindlimb +20°); and coupled forelimb/hindlimb asymmetry (yellow), with tail fixed at 0° (left forelimb +20° −20°, right forelimb −20° and hindlimb +20°). (**b**) The twist left side of the wing produces a higher lift force than the right wing, which induces a roll motion to the right around body's $x$ axis. (**c**) Balance data were collected for the three morphing roll-control strategies at 9 m/s and 10° angle of attack. **d**, **e** Roll angle and roll rate from the open-loop dynamic flight tests; the vertical dashed line indicates the timing of actuator command input. Source data are provided as a Source data file.

relative speeds of the left and right motors, the vehicle achieves active yaw control via differential thrust. When the forelimbs rotated downward and the hindlimbs upward—effectively reducing wing twist—the degree of directional instability was significantly alleviated, with $C_{n\beta}$ decreasing from 0.08 to approximately 0 as the twist was reduced. This improvement arises because changes in wing twist modify the projected side area distribution relative to the center of gravity; coordinated actuation of the fore- and hindlimbs shifts this distribution aft, generating a stabilizing yawing moment. By contrast, varying dihedral alone had a negligible effect on directional stability, with $C_{n\beta}$ remaining nearly constant around 0.05 despite increased dihedral.

## Whole-body morphing induces roll and pitch agility

The SquirrelDrone's high morphing capability significantly enhances its agility, here defined as the ability to change angular rates. Agility is quantified by measuring angular accelerations in pitching, rolling, or yawing motions[1] (see "Agility metric" in Methods). Angular acceleration is defined as the aerodynamic moment (pitch, roll, or yaw) divided by the corresponding moment of inertia. Thus, agility increases when aerodynamic moments are large when inertia is fixed. To evaluate the influence of limb and tail morphing on agility, we adopted two complementary approaches. First, balance measurements in the wind tunnel were used to quantify the aerodynamic moments generated by symmetric fore- and hindlimb actuation, tail morphing, and asymmetric limb actuation (Figs. 6a and 7a). Second, open-loop dynamic flight tests were conducted in the wind tunnel (see "Open-loop dynamic flight test in wind tunnel" in Methods), during which the aircraft was tethered at its center of gravity and commanded with specific limb and tail deflections. These tests directly captured the time-resolved roll and pitch responses, providing a dynamic perspective on agility.

We first consider how roll moments are generated in our morphing-wing design. In conventional fixed-wing aircraft, roll moments are typically produced by asymmetric deflections of ailerons: for example, to initiate a right roll, the left aileron is deflected downward to increase lift on the left wing, while the right aileron is deflected upward to reduce lift on the right wing, thereby creating a rolling moment. For two fixed-wing aircraft with identical inertial properties (same force length), the configuration that generates a larger lift differential between the left and right wings produces a larger rolling moment. In contrast, the SquirrelDrone does not rely on discrete ailerons. Instead, it achieves roll control by inducing wing twist through differential actuation of the forelimbs and hindlimbs, individually or in combination (Fig. 6a). Wind tunnel balance measurements at an angle of attack of 10° showed that the hindlimbs provided higher roll control effectiveness, with $C_{l,\delta_{\mathrm{roll},2}} = 0.134$, compared to $C_{l,\delta_{\mathrm{roll},1}} = 0.088$ for the forelimbs. When fore- and hindlimbs were actuated in differential combination, the highest roll agility was achieved, with $C_{l,\delta_{\mathrm{roll},3}} = 0.190$. This difference arises because in lift-enhancing deformations, downward hindlimb motion generates larger camber changes than upward forelimb motion (Fig. 4e). Moreover, the hindlimbs act on the aft portion of the flow field, producing stronger flow deflections and thereby larger lift increments. When fore- and hindlimbs are actuated in opposite directions, these effects combine to further increase the lift differential and produce the strongest rolling moments.

Open-loop flight tests further validated the effectiveness of these three roll-control strategies. The measured roll angle responses (Fig. 6d) confirmed the differences in roll agility observed in the balance data. Examination of the roll rate responses revealed an interesting transient effect. For instance, during a commanded right roll, the left forelimb deflects upward to increase lift on the left wing. However, the rapid upward motion of the forelimb initially reduces the effective angle of attack due to the relative downward airflow, causing a brief reduction in lift and producing a transient left-roll moment. This results in an initial dip in roll rate (Fig. 6e, blue line) before the flow stabilizes and the right-roll moment dominates. In contrast, hindlimb deflection benefits from this dynamic process. During a right-roll maneuver, lowering the left hindlimb increases the local angle of attack, thereby augmenting lift and strengthening the right-roll response. When fore- and hindlimbs are actuated in opposite directions, a similar transient effect occurs, but the positive contribution from the hindlimbs mitigates the temporary loss of lift from the forelimbs, resulting in an overall stronger roll performance.

https://doi.org/10.1038/s41467-026-72822-w

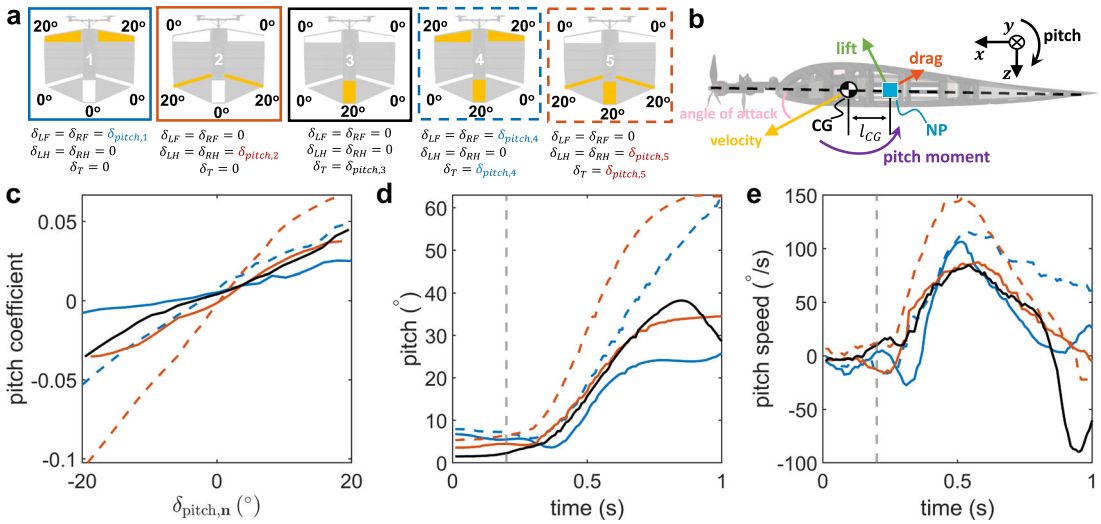


**Fig. 7 | High morphability enhances pitch agility. a** Open-loop dynamics were tested in the wind tunnel at 9 m/s under symmetric wing morphing (see "Open-loop dynamic flight test in wind tunnel" in Methods). Five experimental configurations were applied: forelimb actuation only (solid blue), with hindlimbs and tail fixed at 0° (forelimbs +20°); hindlimb actuation only (solid red), with forelimbs and tail fixed at 0° (hindlimbs +20°); tail only (solid black), with limbs at 0° (tail +20°); coupled forelimb/tail (dash blue) with hindlimbs at 0° (forelimbs and tail at +20°); and coupled hindlimb/tail (dash red) with forelimbs fixed at 0° (hindlimbs and tail at +20°). **b** The lift forces of wing act away from the center of gravity by the wing moment arm, causing a pitching moment around the body's *y* axis. (**c**) Balance data were collected for the five morphing pitch-control strategies at 9 m/s and 10° angle of attack. **d**, **e** pitch angle and pitch speed from the open-loop dynamic flight tests; the vertical dashed line indicates the timing of actuator command input. Source data are provided as a Source data file.

In conventional fixed-wing aircraft, pitch control is typically achieved through deflections of the horizontal tail. The longitudinal pitching moment arises from the relative positions of the neutral point (NP) and the center of gravity (CG)[27]. When the NP lies aft of the CG, lift generated behind the CG produces a stabilizing nose-down moment, whereas if the NP lies forward of the CG, the same aerodynamic force results in a destabilizing nose-up moment. Thus, the magnitude and direction of the pitching moment are governed by both the aerodynamic force and its lever arm relative to the CG (Fig. 7b).

In the SquirrelDrone, pitch control is realized not only through the forelimbs but also through the hindlimbs and tail, which act at larger longitudinal distances from the CG. Wind tunnel measurements demonstrated that both the hindlimbs and the tail generate stronger pitching moments than the forelimbs (Fig. 7c), owing to their longer moment arms relative to the CG. When tail actuation was combined with either forelimb (Fig. 7c, dashed blue line) or hindlimb (Fig. 7c, dashed red line) actuation, pitch authority was further enhanced: the tail not only contributes additional moment due to its extreme aft position but also modifies the overall aerodynamic load distribution along the body. In contrast, the forelimbs, being located closer to the CG, produce weaker pitching moments even for comparable lift increments.

Interestingly, to generate a nose-up pitching moment, all three effectors (forelimbs, hindlimbs, and tail) rotate upward. However, their aerodynamic responses differ: forelimb deflection increases lift with angle of attack (Fig. 4g, blue line), whereas tail and hindlimb deflections lead to a reduction in lift during pitch-up motion (Fig. 4g, red line). This opposite response enhances the overall pitch control authority—while the forelimbs provide a lift increment forward of the CG, the hindlimbs and tail produce lift decrements aft of it, together generating a larger nose-up pitching moment. To verify the effectiveness of these combined mixers (Fig. 7a), we conducted open-loop pitch control tests. The measured pitch angle and rate responses confirmed the predicted differences in control effectiveness among the configurations (Fig. 7d, e), with hindlimb-tail yielding the highest pitch agility.

Although roll and pitch are independently actuated in conventional fixed-wing aircraft, the use of whole-body morphing introduces inherent coupling between these axes. Specifically, deflections of the forelimbs and hindlimbs affect both the local dihedral (influencing roll) and camber/angle of attack (influencing pitch). For instance, during asymmetric hindlimb actuation to induce a right roll, the downward deflection of the left hindlimb not only increases local lift (and thus roll moment), but also produces a nose-down pitching moment due to its position aft the CG. Similarly, symmetric forelimb actuation intended for pitch control can alter lateral stability by modifying wing dihedral.

This coupling was evident in our open-loop wind tunnel tests. In some configurations, a pure roll command generated measurable pitch responses, and vice versa. However, these effects were configuration-dependent and typically weaker than the intended control axis. The observed behaviour underscores a key trade-off in morphing-based flight control: increased flexibility and redundancy at the cost of potential control-axis coupling. In practice, such effects can be mitigated by coordinated mixer design and may even be exploited to enable agile flight.

## Whole-body morphing improves aerodynamic forces and maneuverability

Maneuverability, in this framework, refers to the ability of an aircraft to alter its velocity vector, which depends directly on the linear accelerations acting on the airframe. In the SquirrelDrone, these accelerations are modulated by morphing the limbs and tail, which reshape the aerodynamic surfaces and thereby alter lift and drag. To link these aerodynamic effects with maneuverability, we examined the equations of motion along the flight-path axis under zero-sideslip and no-thrust conditions (see "Maneuverability metric" in Methods). This analysis shows that linear accelerations are governed solely by the resultant lift and drag forces (Fig. 8b), and are maximized when these forces reach their largest magnitudes. Based on this principle, we conducted wind tunnel tests to measure lift (Fig. 8d) and drag (Fig. 8e) under various symmetric limb and tail morphing configurations.

The SquirrelDrone demonstrates substantial increases in both lift and drag by actively adjusting wing twist and the effective angle of attack through limb and tail actuation. Among these, hindlimb actuation (Fig. 8a.3, a.4) proved more effective than forelimb actuation

https://doi.org/10.1038/s41467-026-72822-w

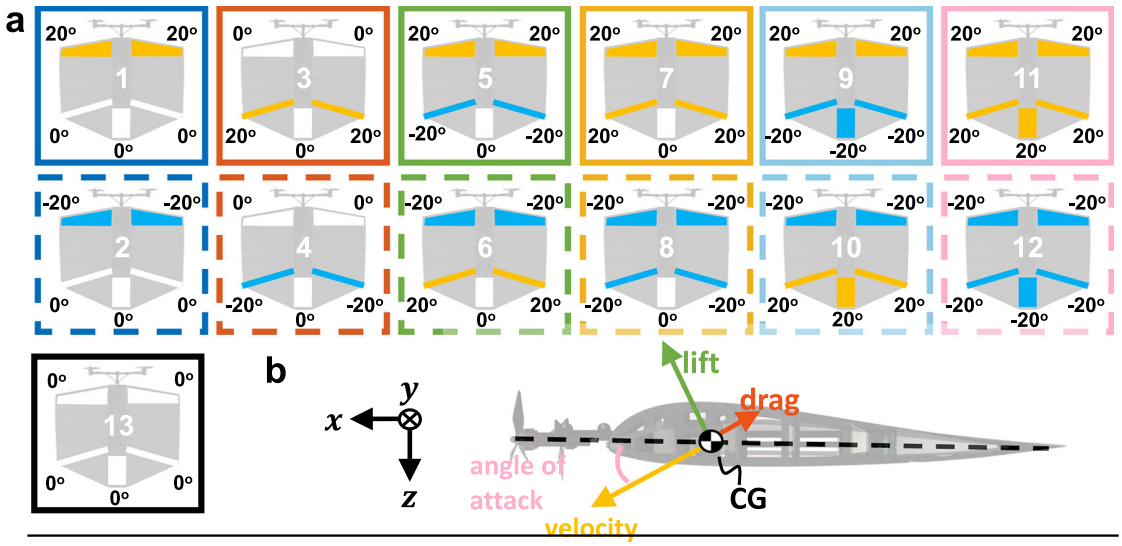


**c** Stall Angles and Maximum Lift Coefficients for the 13 Configuration

| Configurations | 1 | 2 | 3 | 4 | 5 | 6 | 7 | 8 | 9 | 10 | 11 | 12 | 13 |
|---|---|---|---|---|---|---|---|---|---|---|---|---|---|
| Stall angle (deg) | 22 | 36 | 34 | 22 | 20 | 36 | 36 | 30 | 20 | 32 | 36 | 36 | 20 |
| Lift coefficient | 0.86 | 0.83 | 0.65 | 1.29 | 1.17 | 0.71 | 0.72 | 1.13 | 1.23 | 1.26 | 0.65 | 0.61 | 0.78 |

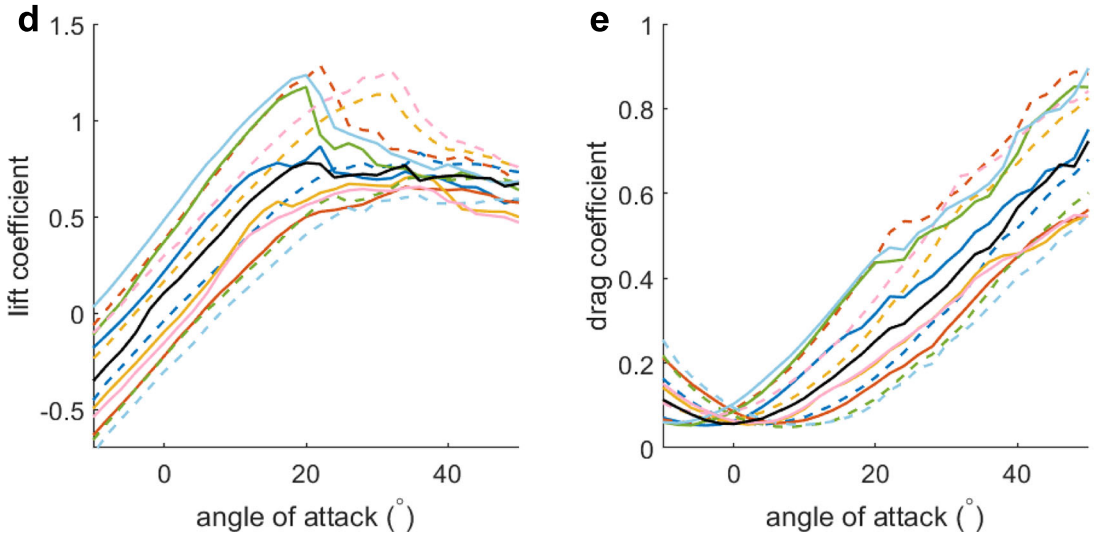


**Fig. 8 | High morphability enhances maneuverability. a** Thirteen configurations in a wind tunnel at 9 m/s, with color and line types indicating various static configurations. **b** Free-body force illustration of the drone's lift and drag force. We presume that the drag force is parallel to the velocity vector, such that the velocity vector deviates from the *x* axis by the angle of attack in the xz plane, while lift is perpendicular to the velocity vector and the *y* axis. (**c**) Angles and maximum lift coefficients for the 13 configurations in (**a**). **d**, **e** Display lift and drag coefficients for the thirteen different configurations across angles of attack ranging from −10° to 50°. Source data are provided as a Source data file.

(Fig. 8a.1, a.2), as the hindlimbs act near the trailing edge, where deformations exert stronger influence on overall camber and pressure recovery. Two primary limb modes were examined: (i) limbs on each side rotating in the same direction (Fig. 8a.7, a.8), which increased lift at higher angles of attack through an anhedral configuration that maintained higher pressure on the lower wing surface; and (ii) limbs rotating in opposite directions (Fig. 8a.5, a.6), which modified the spanwise twist and thus the effective angle of attack, particularly enhancing lift when the forelimbs rotated upward and the hindlimbs downward (Fig. 8a.5), thereby increasing lift near the wingtips. Integrating tail deflection with limb actuation further expanded the range of aerodynamic control (Fig. 8a.9-12), with tail-hindlimb coupling producing the strongest lift and drag augmentation.

The whole-body morphing capability of the SquirrelDrone substantially broadens the range of achievable lift, drag, and pitching moments across a wide spectrum of angles of attack. This capability not only enhances maneuverability but also allows the aircraft to delay stall through active morphological adaptation. As summarized in Fig. 8c, the baseline configuration (Fig. 8a.13) stalled at an angle of attack of approximately 20°, whereas morphing configurations involving coordinated limb and tail actuation (e.g., Fig. 8a.2, a.3, a.6-a.8, a.10-a.12) extended the stall onset beyond 30°. This extension highlights the aerodynamic versatility conferred by whole-body morphing—a key feature underlying the maneuverability of both gliding mammals and their robotic counterparts.

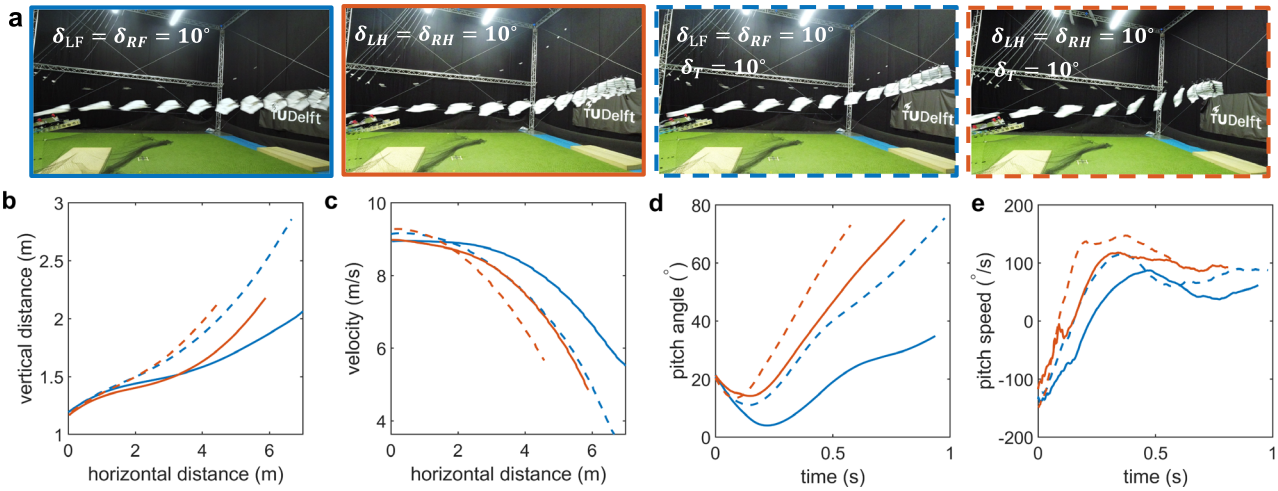


**Fig. 9 | Whole-body morphing enhances flight performance in pull-up flight maneuvers. a** Four indoor pull-up flight tests (see `Pull-up flight test' in Methods and Supplementary Movie 4): forelimbs up 10° (solid blue), forelimbs and tail up 10° (dashed blue), hindlimbs up 10° (solid red), and hindlimbs and tail up 10° (dashed red). The throttle was fixed at 36% in all cases. **b** Flight trajectories of the four configurations. **c** Flight velocity profiles along the trajectories. **d**, **e** Pitch angle and pitch rate during pull-up flight maneuvers. Source data are provided as a Source data file.

### Flight tests

To further validate the flight performance of the SquirrelDrone in real-world conditions, we conducted pull-up flight tests (see "Pull-up flight test setup" in Methods and Supplementary Movies 4 and 5). During these maneuvers, the hindlimbs achieved larger pitch angles earlier than the forelimbs (Fig. 9d, solid red versus solid blue line), consistent with our earlier observation that hindlimbs provide greater pitch agility than forelimbs. This difference can be explained by the fact that the hindlimbs act further aft of the center of gravity, giving them a longer moment arm and therefore greater leverage to generate pitching moments. Moreover, the hindlimbs deform the aft portion of the membrane, which has a stronger influence on camber and effective angle of attack, leading to more pronounced pitch responses. When tail actuation was added to either the forelimbs or hindlimbs, pitch authority was further enhanced (Fig. 9d, e, dashed red and dashed blue lines). The tail contributes additional nose-up or nose-down moments, thereby expanding the available control envelope. Compared with conventional fixed wings, this multi-component morphing strategy enables substantially greater pitch agility and redundancy in control effectiveness.

With respect to maneuverability, the ability to decelerate rapidly during perching is particularly important, as it mitigates impact forces when gliding mammals contact tree trunks. Our results show that hindlimb morphing provided more effective deceleration than forelimb morphing (Fig. 9b, solid red versus solid blue line). This is consistent with the stronger camber changes induced by hindlimbs, which increase drag while simultaneously reducing forward velocity. Adding tail actuation to the limbs further improved this deceleration capability, suggesting that whole-body morphing offers a distributed means of aerodynamic braking. Conversely, when extending glide distance is desirable, forelimb morphing produced longer trajectories than hindlimb morphing (Fig. 9a, solid blue versus solid blue red), owing to its ability to increase lift without a corresponding drag penalty. In addition, tail actuation allowed the aircraft to reach higher altitudes during the pull-up phase (Fig. 9a, dashed blue line), demonstrating its role as a powerful auxiliary control surface.

To evaluate the performance of the SquirrelDrone under realistic outdoor conditions, we conducted a free-flight experiment in an open field subject to moderate gusts (wind up to 10 m/s; see "Outdoor flight test" in Methods and Supplementary Movie 1). The configuration used in this test was selected based on prior wind-tunnel and indoor tests, combining a $\delta^{roll}_{bias} = 10^\circ$ dihedral bias on all limbs for enhanced lateral stability, differential morphing of the forelimbs and hindlimbs for roll control, and symmetric forelimb plus tail actuation for pitch control. Yaw was regulated via differential thrust from the two propellers.

As shown in Fig. 10a, the aircraft achieved a smooth takeoff, followed by a continuous climbing trajectory. During this flight, the vehicle executed a leftward yaw maneuver (from 0 to 7s), followed by a rightward yaw (from 7 to 15s), both induced by RC yaw speed commands and assisted by differential thrust and coordinated roll motion. The roll angle reached up to 47° during the maneuver, while the pitch angle steadily increased, peaking at 42°—demonstrating significant pitch agility and aerodynamic authority in outdoor conditions. Figure 10c–e show the evolution of orientation angles, motor commands, and limb actuation angles, respectively. During the roll and yaw transitions, the actuators performed coordinated asymmetric limb morphing to generate directional moments, validating the morphing-based control logic. Notably, the system remained stable despite turbulent gusts, without any signs of uncontrolled oscillation or structural saturation. This flight serves as a system-level validation of the control strategy developed from earlier experiments. The results confirm that whole-body morphing enables robust, coordinated flight control in unstructured outdoor environments.

## Discussion

Our results demonstrate that whole-body morphing inspired by gliding mammals can substantially enhance the aerodynamic performance and control versatility of small aerial robots. By coordinating the motion of forelimbs, hindlimbs, and tail through a compliant membrane, the SquirrelDrone actively modifies its wing camber, twist, and dihedral in flight, thereby achieving wide-ranging aerodynamic adaptability. This bioinspired morphing strategy enables transitions between flight regimes that traditionally demand conflicting aerodynamic requirements—stable gliding, agile maneuvering.

In contrast to conventional fixed-wing aircraft, where geometry and stability characteristics remain constant once designed, gliding mammals dynamically redistribute aerodynamic loads through coordinated body and limb motion. Our flying-squirrel robot reproduces this biological capability through mechanically simple actuation of five primary effectors, which together emulate the *plagiopatagium*, *propatagium*, and *uropatagium*. Wind tunnel experiments revealed that passive morphing of the ribs increases camber and lift, while active limb control modulates wing twist and dihedral, directly influencing lateral and longitudinal stability. These mechanisms allow the vehicle

https://doi.org/10.1038/s41467-026-72822-w

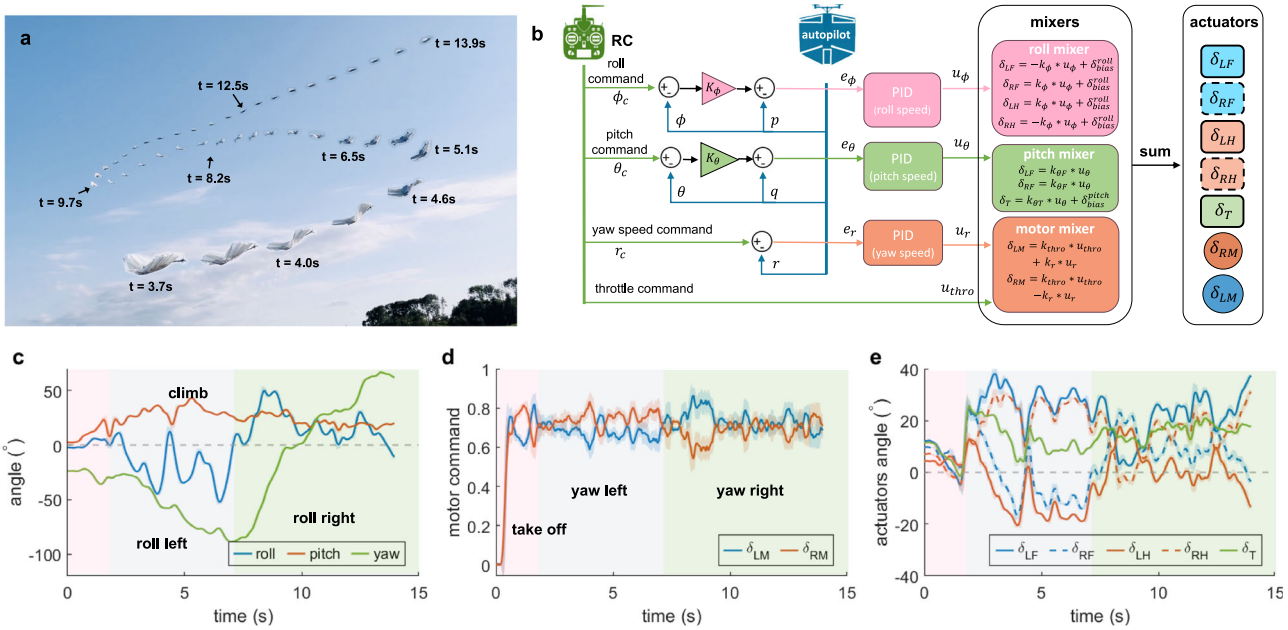


**Fig. 10 | Outdoor flight test. a** Reconstructed trajectory from an outdoor flight trial (see also Supplementary Movie 1). **b** Block diagram of the PID-based control scheme (see "Outdoor flight test" in Methods). The aircraft was manually piloted via RC, with user input for roll, pitch, throttle, and yaw rate commands. Roll control was achieved through differential deflection of the forelimbs and hindlimbs, inducing asymmetric wing morphing. A collective upward deflection offset $\delta_{bias}^{roll}$ was also applied to all limbs to enhance lateral stability. Pitch control was implemented via symmetric forelimb movement in combination with tail actuation. Yaw rate was directly commanded from the RC. Mixer outputs were saturated and mapped to five servo channels and two motors. **c** Roll, pitch, and yaw angles recorded during the flight. **d**, **e** Control inputs sent to the two motors and five servos, respectively. Source data are provided as a Source data file.

to balance between lateral stability and maneuverability in real time, a feature rarely achieved in fixed-wing drones. Unlike conventional aircraft that rely on discrete control surfaces such as ailerons, elevators, and rudders, the SquirrelDrone achieves distributed aerodynamic control through coordinated body morphing. This approach eliminates discontinuities in the aerodynamic surface, reducing flow separation and allowing smooth modulation of lift and pitching moments across the entire span. Whereas fixed-wing designs must trade between static stability and agility at the design stage, the Squirrel can dynamically shift between these states during flight by adjusting limb and tail deflections. This ability to continuously reshape the airframe enables broader control authority with fewer actuators and without the structural penalties associated with traditional control surfaces.

The synergy between the forelimbs, hindlimbs, and tail is critical for this adaptability. Hindlimbs act at larger moment arms and affect the trailing-edge camber, producing stronger aerodynamic moments and higher control effectiveness in both pitch and roll compared with the forelimbs. The tail further augments this control authority by providing additional pitch moments and aerodynamic braking. Such distributed morphing across multiple body segments mirrors the control strategy observed in gliding mammals, which coordinate their limbs and tail to modulate glide path, attitude, and impact velocity during landing.

Beyond static performance, the whole-body morphing architecture enhances both agility and maneuverability. Dynamic wind tunnel and open-loop flight tests showed that limb actuation generates large angular accelerations, while symmetric morphing of limbs and tail increases lift and drag to enable rapid deceleration or high-lift maneuvers. These findings parallel the strategies of flying squirrels and colugos, which increase membrane curvature and tail spread to slow down before perching. In both biological and robotic systems, morphing serves as a distributed means of generating aerodynamic forces rather than relying on discrete control surfaces.

The pull-up experiments highlight how this morphing strategy translates into practical flight capability. By combining hindlimb and tail actuation, the robot achieved steeper trajectories, larger pitch angles, and more effective deceleration, demonstrating that whole-body coordination enhances both control precision and energy dissipation during landing. This behavior closely resembles the controlled body rotation and membrane tensioning employed by gliding mammals to perform soft, accurate landings on vertical surfaces. Conversely, forelimb-driven morphing produced longer trajectories and gentler approaches, illustrating how different limb combinations can be tuned for specific flight objectives.

Taken together, these results suggest that whole-body morphing provides a unifying mechanism to reconcile stability, agility, and maneuverability within a single airframe. The compliant skin and articulated skeleton enable passive aerodynamic adaptation while minimizing mechanical complexity. From a biological perspective, this study provides robotic evidence supporting the aerodynamic function of coordinated limb and tail morphing in gliding mammals. From a robotics standpoint, it offers a design principle for future aerial robots capable of morphing their entire body to seamlessly transition between efficient gliding and agile maneuvering in cluttered environments.

Despite these advantages, several limitations intrinsic to whole-body morphing remain. First, whole-body morphing introduces roll-pitch coupling: asymmetric limb motions generate both lateral and longitudinal moments. Our cascaded SISO (single input single output) PID controller lacks the ability to decouple these effects, reducing precision during aggressive maneuvers. Future work will explore model-based control methods such as incremental non-linear dynamic inversion (INDI) or model predictive control (MPC), which offer better control allocation under redundancy and coupling.

From a design perspective, the low aspect ratio of the wing, inspired by the mammalian gliders, increases induced drag and enhances lateral sensitivity. Dihedral was introduced to improve roll stability, but this reduces lateral control authority. Future designs may increase the aspect ratio or introduce hybrid planforms to better

balance aerodynamic efficiency, control authority, and robustness to wind disturbances.

Lastly, coupling onboard perception with adaptive control to coordinate morphing in real time would unlock robust multi-modal locomotion, enabling seamless gliding-to-landing transitions and autonomous wing stabilization under gust disturbances. Such capabilities would mark a decisive step toward robotic flyers that approach their biological counterparts not only in efficiency, but in adaptability and grace.

## Methods

### Design process

**Biomimetic scaling of aerodynamic parameters.** We designed the SquirrelDrone based on an analysis of morphological and body mass data from 53 species of gliding mammals, as detailed in ref. 5. Our investigation into the relationship between body mass (m) and head and body length (HB, measured from the tip of the snout to the cloaca along the ventral surface) revealed a pronounced quadratic relationship, which we encapsulated in the following model:

$$m = 8.98(\mathrm{HB})^2 - 0.65\mathrm{HB} + 0.01 \tag{1}$$

$$L = 0.5\rho V^2 S C_L \tag{2}$$

Using this equation to guide our design parameters and accounting for the mass of necessary onboard electronic components, we engineered the aircraft with a weight of 0.689 kg and a wingspan of 0.7 m. The average aerodynamic chord was set at 0.52 m. More details see Fig. 2b.

**Passive ribs design.** The soft membrane can morph into different shapes via the 5 rotatable components (4 limbs and 1 tail). To facilitate morphing, three ribs are distributed along the forelimb and hindlimb components (three on each wing). The wing section uses a NACA M5 airfoil, an S-shaped profile, as shown in Fig. 2i. This section, 200 mm from the symmetry plane (indicated by the green dashed line in Fig. 2a), shows the basic NACA M5 in gray background, the forelimb leading-edge in blue, rib positions in green, hindlimb in orange, and the soft membrane in black. The forelimbs and hindlimbs are actively rotated vertically by servos, while the ribs are passively moved by the membrane, whose shape is influenced by the limbs and tail rotation angles and aerodynamic forces, forming the SquirrelDrone's morphing strategy.

**Morphing airframe components.** The main structure of the SquirrelDrone consists of the fuselage's primary frame, forelimbs, ribs, hindlimbs, tail, soft membrane, and propulsion components. The fuselage's primary frame is made of 1 mm CNC-machined carbon fibre plates, precisely aligned and glued together to ensure accurate positioning of actuators and gears (see Fig. 2a). A 10 × 10 mm carbon fibre square tube runs through the fuselage, providing structural integrity and serving as the mounting point for the front-end propulsion system.

The forelimbs (see Figure 2f) and hindlimbs (see Figure 2g) are lightweight PLA-printed structures with a 4 × 4 mm carbon fibre square tube embedded at the center. A 3D-printed gear is installed at the tube's root, and a small bearing is integrated into the gear to minimize rotational friction.

For the ribs (see Fig. 2h), foam is used as the core material, with two 2 mm carbon fibre tubes attached to the upper and lower sides. A 3D-printed connector secures these components, while the carbon fibre tubes facilitate easy adhesion to the membrane. The tail is also constructed from 1 mm CNC-machined carbon fibre plates, ensuring a robust yet lightweight structure.

The propulsion system consists of a single 380 mm long 8 × 8 mm carbon fibre square tube, which is attached to the fuselage using a 3D-printed joint.

Once all components are properly assembled and fixed on the SquirrelDrone frame jig, the membrane can be adhered to the structure. We use an ultra-thin thermoplastic polyurethane (TPU) material (0.01 mm) with high elongation and elastic recovery properties. To ensure better symmetry, the membrane is cut into left-right symmetric pieces and temporarily fixed onto the jig using paper tape. Since most adhesives are somewhat corrosive, we use Gorilla Superglue Gel for bonding. A cotton swab is used to apply a small amount of glue to the designated adhesion points on the membrane and structural components.

**Electronics.** *Actuators:* The SquirrelDrone uses serial-bus servos (FeeTech STS3032) with built-in 12-bit high-precision magnetic encoders for precise gear rotation control. However, due to size constraints, each actuator can handle a maximum load of 4.5 kg cm. The movable limbs and tail are driven by five actuators: two for the forelimbs (Fig. 1S-1, S-2), two for the hindlimbs (S-3, S-4), and one for the tail (S-5). To reduce the load on the servos, we designed specific gear sets for each of the five servos, as shown in Fig. 2b.

*Propulsion system:* The propulsion system includes twin motors (Emax ECO II Series 2207 Motor 1900KV), propellers (5 inch × 4.3 inch × 3), and electronic speed controllers (ESCs, T-Motor F45A 32bit 3-6S ESC), aligned to pass through the center of gravity, thereby providing thrust and yaw control without affecting pitch.

*Autopilot:* The autopilot board used in our system is the Pixracer R15, running the Paparazzi firmware. Two motors receive pulse width modulation (PWM) directly from autopilot. All servos are controlled via a Teensy 4.0 board, which receives actuator commands from the Pixracer through a UART port. The Teensy 4.0 then transmits position commands to five serial servos. See Supplementary Fig. 2.

### Metrics definitions

**Longitudinal stability metric.** Mathematically, an aircraft is considered pitch stable if the slope of the pitch coefficient $C_m$ with respect to the angle of attack $\alpha$ is negative, as defined by:

$$C_{m,\alpha} = \frac{\partial C_m}{\partial \alpha} < 0 \tag{3}$$

Under this condition, the aircraft exhibits stability because the angle of attack passively converges toward a stable equilibrium at $C_m = 0$ following any disturbance. Conversely, if the slope of the pitch coefficient is positive, the angle of attack will diverge from equilibrium, rendering the aircraft unstable.

**Lateral and directional stability metric.** Lateral stability refers to an aircraft's inherent ability to resist disturbances in roll, while directional (or weathercock) stability describes its ability to resist disturbances in yaw. These two components together determine the aircraft's overall stability in sideslip.

If an aircraft experiences a disturbance that induces a roll but does so very slowly, the roll rate can be considered negligible, and no restorative rolling moment will occur unless sideslip is induced. If sideslip generates a restorative rolling moment, the aircraft is laterally stable. Typically, an aircraft is considered laterally stable if the derivative of the rolling moment coefficient with respect to the sideslip angle is less than zero:

$$C_{l\beta} = \frac{\partial C_l}{\partial \beta} < 0 \tag{4}$$

where $C_l$ is the rolling moment coefficient and $\beta$ is the sideslip angle. Factors commonly influencing an aircraft's lateral stability include

wing sweep, dihedral angles, and wing twist[18]. The SquirrelDrone emulates the propatagium of gliding mammals, maintaining a constant 10° sweep angle during morphing, which contributes to enhanced lateral stability. When the forelimbs and hindlimbs both deflect upwards, this increases the aircraft's dihedral angle. Conversely, when they deflect in opposite directions, the twist of the wing is altered.

Directional or weathercock stability characterizes the aircraft's tendency to align itself with the oncoming airflow following a yaw disturbance. A directionally stable configuration generates a restorative yawing moment when a sideslip occurs, driving the nose back into the wind. This behavior is quantified by the weathercock stability derivative:

$$C_{n\beta} = \frac{\partial C_n}{\partial \beta} \tag{5}$$

where $C_n$ is the yawing moment coefficient. For a stable configuration, $C_{n\beta}$ should be less than zero, indicating that the yawing moment acts to oppose the sideslip. Factors that improve directional stability include vertical tail area, fuselage side area aft of the center of gravity, and wing dihedral or sweep effects[18].

In the SquirrelDrone, the absence of a conventional vertical tail leads to reduced directional stability, consistent with the predominantly planar morphology of gliding mammals. Adjusting the relative deflection of the forelimbs and hindlimbs modifies the effective side area distribution, thereby influencing $C_{n\beta}$. For example, opposite deflections of the fore- and hindlimbs alter the projected planform and can partially compensate for the lack of a vertical stabilizing surface, improving weathercock stability under certain morphing configurations.

**Agility metric.** Agility is defined as the capability to achieve high controlled angular rates in roll $\dot{p}$, pitch $\dot{q}$, and yaw $\dot{r}$, revolving around the drone's body-fixed axes. To accurately assess external factors that influence agility, we simplified the kinematic equations of motion to concentrate exclusively on pure rotation, as detailed in ref. 28:

$$\begin{pmatrix} \dot{p}_p \\ \dot{q}_p \\ \dot{r}_p \end{pmatrix} = \begin{pmatrix} \frac{P}{I_{xx}} \\ \frac{Q}{I_{yy}} \\ \frac{R}{I_{zz}} \end{pmatrix} \tag{6}$$

In this model, $P$, $Q$, and $R$ represent the moments about the roll, pitch, and yaw axes, respectively. The denominators $I_{xx}$, $I_{yy}$, and $I_{zz}$ are the moments of inertia about the respective $x$, $y$, and $z$ axes. This framework allows for precise quantification of the drone's agility, indicating that greater moments under similar aerodynamic angles result in superior agility. To compare the torque variations brought by different combinations of limbs and tail mixers, we characterize the changes in roll and pitch moment coefficients per unit actuator angle using $C_{l,\delta_n}$ and $C_{m,\delta_n}$, as follows:

$$C_{l,\delta_n} = \frac{\partial C_l}{\partial \delta_n} \tag{7}$$

$$C_{m,\delta_n} = \frac{\partial C_m}{\partial \delta_n} \tag{8}$$

Here, $C_l$ represents the roll coefficient and $C_m$ represents the pitch coefficient, with $\delta_n$ corresponding to the actuator angle for the configuration noted in Fig. 3a.

**Maneuverability metric.** Maneuverability is defined as the ability to achieve controlled, high linear accelerations, enabling rapid changes in both the speed and direction of the aerial vehicle's translational movement[7]. For rigorous assessment within a wind-fixed reference frame, maneuverability is mathematically represented as:

$$\begin{pmatrix} \ddot{x} \\ \ddot{y} \\ \ddot{z} \end{pmatrix} = \begin{pmatrix} \frac{-D}{m} - g\sin\gamma \\ -\frac{L\sin\varphi}{m} \\ \frac{L\cos\varphi}{m} - g\cos\gamma \end{pmatrix} \tag{9}$$

where $D$ is the drag force, $L$ is the lift force, $m$ is the mass of the drone, $g$ represents gravitational acceleration, $\gamma$ is the longitudinal flight path angle, and $\varphi$ is the bank angle. This formulation allows for precise quantification of maneuverability under varying flight conditions.

## Data collection

**Membrane-based deformation tracking.** We conducted morphing experiments and balance data collection at the Open Jet Facility (OJF) at Delft University of Technology. The OJF, a low-speed closed-circuit wind tunnel, occupies a large room with dimensions of 13 m in width and 8 m in height. It features a state-of-the-art motion-tracking system equipped with 16 cameras. A total of 95 reflective markers were precisely placed on the upper surface of the drone, each tracked individually by the motion-tracking system at a frequency of 360 Hz. The strategic placement of these markers included seven points on the forelimb, three points on each end and the middle of the ribs, four points on the leg, and four markers each on membranes 1–4. Additionally, the membrane between the leg and tail had five markers, the middle front half of the fuselage had ten markers, and the tail had five markers. High-speed sports cameras were also used to record the experiments, capturing footage at 240 frames per second with a resolution of 1920 × 1080 pixels.

**Camber and chord measurements.** In this study, the camber of the membrane wing was defined using a simplified geometric approach. For each cross-sectional profile, a baseline chord line was constructed by connecting the leading-edge and trailing-edge points of the wing. The chord length ($c$) was defined as the straight-line distance between these two points. The maximum camber ($C_{\max}$) was determined as the largest vertical distance from the upper surface of the membrane to this chord line[29]. The camber ratio was then calculated as

$$C_r = \frac{C_{\max}}{c}, \tag{10}$$

where $c$ is the chord length. This definition provides a consistent measure of membrane deformation across different morphing states, while avoiding the complexity of computing the mean camber line for flexible and non-rigid wing surfaces.

**Angle of attack measurements.** In this study, the angle of attack (AoA) of the SquirrelDrone was defined based on the orientation of the wing relative to the incoming flow. The overall, or body-level, AoA was determined from the aerodynamic angle of the wing root section, located at the midspan and aligned with the fuselage, and is therefore referred to as the aircraft's angle of attack.

Local airfoil angle were also defined at specific spanwise positions to characterize the aerodynamic deformation of the membrane wing. For instance, the AoA at $y$ = 300 mm was calculated as the angle between the chord line—connecting the foremost and rearmost points of the wing section at that spanwise location—and the freestream direction.

In practice, these angles were obtained from the reconstructed wing geometry using motion-capture (MoCap) data. The upper-surface markers were tracked to reconstruct the three-dimensional shape of the wing, from which both global and local angles of attack were derived.

**Wind tunnel experimental set-up.** We conducted morphing-state-locked polar analysis wind tunnel tests at the Open Jet Facility (OJF) at Delft University of Technology. The aircraft's angle of attack was adjusted using a Xiaomi Cybergear robotic motor, and a balance sensor (ATI F/T sensor: mini45) was fixed directly beneath the aircraft's center of gravity. A serial cable connected the aircraft's servo controller (Teensy 4.0) to a laptop computer, which used the Robot Operating System (ROS[30]) to generate and transmit angle commands for the bus servos to the aircraft. Both the motor controlling the angle of attack and the balance sensor were also integrated into ROS. To more accurately study the aerodynamic effects of a morphing wing, we did not install a propulsion system in the wind tunnel tests for this paper.

We conducted three types of morphing-state-locked polar analysis wind tunnel tests at OJF. The first type focused on testing the advantages of a passive membrane. For these tests, servo positions for the limbs and tail were set to 0 degrees, and the OJF wind speed was incrementally increased from 3 m/s to 12 m/s in 1 m/s steps. After each wind speed reached stability, we collected approximately 30 s of balance data, motion tracking data, and actuator data. The second type involved tests with all actuator commands set to zero, where wind speeds were stabilized at 6 m/s, 9 m/s, and 12 m/s. At these speeds, we examined both passive and fixed ribs across a range of angles of attack from −10° to 50°, at 2° increments, collecting data for 6 seconds at each stable angle. The third type, corresponding to predefined actuator commands shown in Fig. 3, involved data collection at a constant wind speed of 9 m/s, where angles of attack varied from −10° to 50° in 2° steps.

In addition, we conducted limb-tail actuation-driven wind tunnel tests. We stabilized the wind speed at 9 m/s and fixed the angle of attack at 10 degrees. Following the configurations provided in Figs. 6a and 7a, commands were issued to the servos controlling the forelimbs and hindlimbs, with their ranges set from −20 degrees to 20 degrees. The tail's range was set from −30 degrees to 30 degrees, with all adjustments made in 2-degree increments. For each change in configuration, we collected 6 s of data, including balance data, motion tracking system data, and actuator feedback data.

For analyzing aerodynamic forces and moments in wind tunnel tests, we employed a MATLAB script to compute the averages and standard deviations of these measurements over intervals of 6 or 30 s. Additionally, we normalized the results according to the standard nondimensional coefficients referenced in ref. 31:

$$C_L = \frac{2L}{\rho S V^2} \tag{11}$$

$$C_D = \frac{2D}{\rho S V^2} \tag{12}$$

$$C_m = \frac{2M}{\rho S c V^2} \tag{13}$$

$$C_l = \frac{2N}{\rho S b V^2} \tag{14}$$

Here, $L$ denotes lift force, $D$ drag force, $M$ pitch moment, and $N$ roll moment. $V$ represents airspeed, $S$ is the wing area, $\rho$ is air density, $c$ is the mean aerodynamic chord (with $c$ = 0.52 m), and $b$ is the wingspan (with $b$ = 0.7 m). SquirrelDrone morphs by alternating the positions of its limbs and tail, keeping the wing area relatively constant at 0.356 $m^2$.

**Open-loop dynamic flight experiment in the wind tunnel.** To evaluate the agility of the SquirrelDrone, open-loop dynamic flight tests were conducted in the Open Jet Facility (OJF) at Delft University of Technology. For safety, the aircraft was tethered at its center of gravity using a thin line and suspended within the test section. The wind speed was gradually increased from 3 m/s and stabilized at 9 m/s. Using a remote controller (RC) in attitude stabilization mode, the aircraft was first trimmed to a stable condition. Subsequently, specific deflections of the limbs and tail were commanded (Figs. 6a and 7a), while attitude data were recorded from the onboard autopilot. Each configuration was repeated five times to ensure repeatability.

The open-loop setup was chosen to isolate the direct aerodynamic response of limb and tail actuation, avoiding interference from feedback control and thereby providing a clearer assessment of the intrinsic agility characteristics of the morphing-wing design.

**Pull-up flight experiment setup.** Pull-up tests were conducted in the Cyberzoo indoor flight arena at Delft University of Technology. The indoor environment was chosen to eliminate outdoor wind disturbances, enabling more reliable comparisons between control strategies and allowing accurate position tracking. The aircraft was launched using a custom launcher based on rubber propulsion, providing an initial velocity of 9 ± 0.3 m/s. The launcher was set at an angle of 25°, with the aircraft aligned at 0° relative to the launch rail. The aircraft position was tracked by a motion capture (MoCap) system operating at 150 Hz. Immediately after leaving the launcher, the propellers were engaged and stabilized at 36% throttle. To ensure fair comparison across control strategies, all control inputs were preprogrammed and executed automatically by the onboard flight controller (Pixracer R15), with limb and tail positions set before placement on the launch rail. Flight data were collected from two sources: position measurements from the MoCap system and onboard flight logs recorded on the Pixracer R15 SD card. Data analysis was performed in MATLAB.

**Outdoor flight experiment.** To evaluate flight performance in real-world conditions, we conducted an outdoor free-flight experiment in Valkenburg, Netherlands. The test took place on a windy winter afternoon, under demanding atmospheric conditions. Meteorological records from the Dutch Royal Weather Institute (KNMI) reported average wind speeds of 3.6–3.9 m/s, with sustained hourly peaks up to 6.0 m/s and gusts reaching 10.0 m/s. The wind direction was predominantly west-southwest (258°), resulting in strong crosswind components at the test field.

The SquirrelDrone was hand-launched and flown manually in RC mode. To enhance lateral stability under wind disturbances, all four limbs were preset with a $\delta_{\text{bias}}^{\text{roll}} = 10^\circ$ upward bias to increase effective dihedral, as supported by our prior wind tunnel findings. The vehicle performed a continuous climb while executing coordinated left and right turns (see Supplementary Movie 1 and Fig. 10a).

As shown in Fig. 10b, the onboard attitude controller followed a cascaded architecture. The outer loops for roll and pitch used proportional (P) controllers to compute attitude errors relative to the RC commands. The inner loops applied full PID control to track angular velocity. Yaw rate was regulated by a single-layer proportional controller. Control errors were passed to a mixer that converted roll, pitch, and yaw demands into actuator-level commands for the limbs and motors.

**Outer-loop (attitude error):**

$$e_\phi = K_\phi(\phi_c - \phi) - p \tag{15}$$

$$e_\theta = K_\theta(\theta_c - \theta) - q \tag{16}$$

$$e_r = r_c - r \tag{17}$$

**Inner-loop (angular rate control):**

$$u_\phi = \mathrm{PID}_\phi(e_\phi) \tag{18}$$

$$u_\theta = \mathrm{PID}_\theta(e_\theta) \tag{19}$$

$$u_r = \mathrm{PID}_r(e_r) \tag{20}$$

**Mixer (control allocation):**

$$u_{\mathrm{LF}} = -k_\phi u_\phi + \delta_{\mathrm{bias}}^{\mathrm{roll}} + k_{\theta\mathrm{F}} u_\theta \tag{21}$$

$$u_{\mathrm{RF}} = k_\phi u_\phi + \delta_{\mathrm{bias}}^{\mathrm{roll}} + k_{\theta\mathrm{F}} u_\theta \tag{22}$$

$$u_{\mathrm{LH}} = k_\phi u_\phi + \delta_{\mathrm{bias}}^{\mathrm{roll}} \tag{23}$$

$$u_{\mathrm{RH}} = -k_\phi u_\phi + \delta_{\mathrm{bias}}^{\mathrm{roll}} \tag{24}$$

$$u_{\mathrm{T}} = k_{\theta\mathrm{T}} u_\theta + \delta_{\mathrm{bias}}^{\mathrm{pitch}} \tag{25}$$

$$u_{\mathrm{LM}} = k_{\mathrm{thro}} u_{\mathrm{thro}} + k_r u_r \tag{26}$$

$$u_{\mathrm{RM}} = k_{\mathrm{thro}} u_{\mathrm{thro}} - k_r u_r \tag{27}$$

Here, $u_{\mathrm{thro}}$ denotes the throttle input from the RC, ranging from 0 to 1. $\delta_{\mathrm{bias}}^{\mathrm{pitch}}$ is pitch trim. Subscripts LF, RF, LH, RH, and T refer to the left/right forelimbs, hindlimbs, and tail, respectively; LM and RM refer to the left and right motors.

## Data availability

The datasets generated and analyzed during this study are publicly available in the Zenodo repository at https://doi.org/10.5281/zenodo.19052718. Source data are provided with this paper.

## Code availability

The code used for the flight control system and servo actuation is available in the repository at https://doi.org/10.5281/zenodo.19053195.

## References


1. Ajanic, E., Feroskhan, M., Mintchev, S., Noca, F. & Floreano, D. Bioinspired wing and tail morphing extends drone flight capabilities. *Sci. Robot.* **5**, eabc2897 (2020).
2. Chang, E., Matloff, L. Y., Stowers, A. K. & Lentink, D. Soft biohybrid morphing wings with feathers underactuated by wrist and finger motion. *Sci. Robot.* **5**, eaay1246 (2020).
3. Chen, A., Song, B., Wang, Z., Xue, D. & Liu, K. A novel actuation strategy for an agile bioinspired fwav performing a morphing-coupled wingbeat pattern. *IEEE Trans. Robot.* **39**, 452–469 (2022).
4. Bahlman, J. W., Swartz, S. M., Riskin, D. K. & Breuer, K. S. Glide performance and aerodynamics of non-equilibrium glides in northern flying squirrels (Glaucomys sabrinus). *J. R. Soc. Interface* **10**, 20120794 (2013).
5. Jackson, S. *Gliding Mammals of the World* (CSIRO Publishing, 2012).
6. Verbeke, J. & Schutter, J. D. Experimental maneuverability and agility quantification for rotary unmanned aerial vehicle. *Int. J. Micro Air Veh.* **10**, 3–11 (2018).
7. Dudley, R. Mechanisms and implications of animal flight maneuverability. *Integr. Comp. Biol.* **42**, 135–140 (2002).
8. Li, D. et al. A review of modelling and analysis of morphing wings. *Prog. Aerosp. Sci.* **100**, 46–62 (2018).
9. Lingling, C. et al. Design, modeling, and control of morphing aircraft: a review. *Chin. J. Aeronaut.* **35**, 220–246 (2022).
10. Chang, E., Chin, D. D. & Lentink, D. Bird-inspired reflexive morphing enables rudderless flight. *Sci. Robot.* **9**, eado4535 (2024).
11. Phan, H.-V. & Floreano, D. A twist of the tail in turning maneuvers of bird-inspired drones. *Sci. Robot.* **9**, eado3890 (2024).
12. Rodrigue, H. et al. Effect of twist morphing wing segment on aerodynamic performance of UAV. *J. Mech. Sci. Technol.* **30**, 229–236 (2016).
13. Garcia, H., Abdulrahim, M. & Lind, R. Roll control for a micro air vehicle using active wing morphing. In *Proc. AIAA Guidance, Navigation, and Control Conference and Exhibit* 5347 (AIAA, 2003).
14. Jenett, B. et al. Digital morphing wing: active wing shaping concept using composite lattice-based cellular structures. *Soft Robot.* **4**, 33–48 (2017).
15. Ramezani, A., Chung, S.-J. & Hutchinson, S. A biomimetic robotic platform to study flight specializations of bats. *Sci. Robot.* **2**, eaal2505 (2017).
16. Anderson, J. *EBOOK: Fundamentals of Aerodynamics (SI units)* (McGraw-Hill, 2011).
17. Thorington Jr, R. W. & Heaney, L. R. Body proportions and gliding adaptations of flying squirrels (petauristinae). *J. Mammal.* **62**, 101–114 (1981).
18. Pamadi, B. N. *Performance, Stability, Dynamics, and Control of Airplanes* (AIAA, 2004).
19. Jackson, S. M. Glide angle in the genus petaurus and a review of gliding in mammals. *Mammal. Rev.* **30**, 9–30 (2000).
20. Sharma, A. & Visbal, M. Numerical investigation of the effect of airfoil thickness on onset of dynamic stall. *J. Fluid Mech.* **870**, 870–900 (2019).
21. Byrnes, G., Lim, N. T.-L. & Spence, A. J. Take-off and landing kinetics of a free-ranging gliding mammal, the malayan colugo (Galeopterus variegatus). *Proc. R. Soc. B Biol. Sci.* **275**, 1007–1013 (2008).
22. Thorington Jr, R. W., Darrow, K. & Betts, A. D. Comparative myology of the forelimb of squirrels (sciuridae). *J. Morphol.* **234**, 155–182 (1997).
23. Oxnard, C. E. The architecture of the shoulder in some mammals. *J. Morphol.* **126**, 249–290 (1968).
24. Kumkam, N., Suratemeekul, N. & Sleesongsom, S. A new conceptual design of twisting morphing wing. *Biomimetics* **10**, 110 (2025).
25. Sofla, A., Meguid, S., Tan, K. & Yeo, W. Shape morphing of aircraft wing: status and challenges. *Mater. Des.* **31**, 1284–1292 (2010).
26. Vos, R., Gürdal, Z. & Abdalla, M. Mechanism for warp-controlled twist of a morphing wing. *J. Aircr.* **47**, 450–457 (2010).
27. Harvey, C., Baliga, V. B., Wong, J. C., Altshuler, D. L. & Inman, D. J. Birds can transition between stable and unstable states via wing morphing. *Nature* **603**, 648–653 (2022).
28. Nelson, R. C. et al. *Flight Stability and Automatic Control* (WCB/McGraw-Hill, 1998).
29. Song, A. et al. Aeromechanics of membrane wings with implications for animal flight. *AIAA J.* **46**, 2096–2106 (2008).
30. Quigley, M. et al. Ros: an open-source robot operating system. In *Proc. ICRA Workshop on Open Source Software* (ICRA, 2009).
31. Phillips, W. F. *Mechanics of Flight* (John Wiley & Sons, 2004).


## Acknowledgements

The authors thank Erik van der Horst for piloting the drone during outdoor flight tests; Anton Lang for assistance with the autopilot development and wind tunnel testing; Baihui Chen, Ziqing Ma, Yiyuan Zou, Hang Yu, Yilun Wu, Yujie Wang, Chaoxiang Ye, Dequan Ou, Xiaoyan Bai, and Shenqi Wang for their assistance with the wind tunnel experiments; and Peter Duyndam, Dennis Bruikman, and Ferdinand Schrijer from the Delft University of Technology Open Jet wind tunnel facility for technical support. This research received no specific funding.

## Author contributions

Conceptualization of the study: S.Hamaza and L. Zheng. Prototype Building: L. Zheng and S. Hamaza. Aerodynamic Design: L. Zheng and A.V. Zuijlen. Experiments: L. Zheng. Data Processing: L. Zheng. Visuals: L. Zheng and S. Hamaza. Funding: S. Hamaza. Writing of the original draft: L. Zheng and S. Hamaza. Draft revision and editing: L. Zheng, S. Hamaza and A.V. Zuijlen.

## Competing interests

The authors declare no competing interests.

## Additional information

**Supplementary information** The online version contains supplementary material available at https://doi.org/10.1038/s41467-026-72822-w.

**Correspondence** and requests for materials should be addressed to Liming Zheng or Salua Hamaza.

**Peer review information** *Nature Communications* thanks the anonymous reviewers for their contribution to the peer review of this work. A peer review file is available.